Nitrogen-seeded impurity emission front control experiments in TCV

J.T.W. Koenders[1,2], A. Perek[3], B. Kool[1,2], O. Février[3], T. Ravensbergen[4], C. Galperti[3], B.P. Duval[3], C. Theiler[3], M. van Berkel[1], the TCV team[a] and the EUROfusion MST1 team[b]

[1] DIFFER - Dutch Institute for Fundamental Energy Research, Eindhoven, Netherlands
[2] Department of Mechanical Engineering, Control Systems Technology Group, Eindhoven University of Technology, Eindhoven, Netherlands
[3] École Polytechnique Fédérale de Lausanne (EPFL), Swiss Plasma Center (SPC), Lausanne, Switzerland
[4] ITER Organization, St. Paul Lez Durance Cedex, France
[a] See author list of H. Reimerdes *et al.,* Nucl. Fusion **62**, 042018 (2022)
[b] See author list of B. Labit *et al.,* Nucl. Fusion **59**, 086020 (2019)

E-mail: `j.t.w.koenders@differ.nl`

Abstract. This paper presents the first result using nitrogen-seeded exhaust feedback control of the NII impurity emission front in TCV. The NII emission front position is consistently located below its commonly used CIII counterpart, indicating the NII emission front is representative of a colder plasma region. We demonstrate control of the NII impurity emission front position for two cases: 1) using nitrogen seeding as the sole actuator, and 2) using deuterium fueling as an actuator while injecting a small amount of nitrogen that remains a trace impurity. For sole nitrogen actuation, peak target current density is significantly reduced when the NII emission front approaches the x-point ($\approx 50\%$ for the NII front at the halfway point). When actuating with deuterium, peak target current density is less affected, which is explained by changes in fueling engendering a different scrape-off-layer plasma density. Perturbative (system identification) experiments show that nitrogen actuation induces a stronger, but slower, response of the NII emission front than deuterium actuation. Moving the NII emission front back to the target after pushing it towards the x-point is proven difficult, where both the NII front position and total radiated power do not reach pre-seeding conditions within the discharge time following termination of nitrogen injection. This result highlights the need to account for impurity retention in such seeded discharges in exhaust control strategies, actively measuring impurity enrichment of the divertor plasma.

Submitted to: *Nuclear Fusion*

31 August 2022

1. Introduction

One of the major outstanding challenges for reactor relevant tokamak operation is the heat and particle load on the first wall, notably the divertor [1]. Left unmitigated, the expected power fluxes impacting the divertor targets during reactor-relevant operation exceed present-day materials engineering limits [2, 3]. Real-time feedback control of plasma detachment, a regime characterized by a large reduction of plasma temperature and plasma pressure at the divertor target, is required to maintain a sufficient reduction of these fluxes [4, 5].

Designing such exhaust feedback controllers systematically requires a dynamic (time-dependent) model of the to be controlled physical system and the used actuators and sensors, allowing model-based guarantees on stability and performance to be given [6]. Predictive dynamic models are therefore paramount to confidentially apply controllers to a new reactor from the first discharge, starting with a robust design in the robustness-performance trade-off, and moving to performance design once more experimental data is available to validate or improve the modeled dynamics. Experimental identification of the heat exhaust dynamics is therefore the logical approach to design controllers for present-day devices, both ensuring discharge efficient control development and extending the experimental database for dynamic model validation.

In [7], dedicated *system identification* experiments were performed to obtain a parametric dynamic model of the CIII (465 nm triplet) emission front position response to deuterium (D_2) fueling in the carbon machine Tokamak à Configuration Variable (TCV). This model was used to systematically design a controller off-line, resulting in successful real-time feedback control of the CIII emission front, where the intrinsic Carbon of the TCV wall allowed for enhanced radiation. In future reactors, which will most likely require metal walls, intrinsic impurity radiation from carbon will not be present. Therefore, exhaust control will require the direct injection of impurities into the divertor region to augment power losses before the divertor plates, as envisioned for ITER and DEMO [8, 9].

In this paper, we adhere to this approach, performing real-time plasma exhaust control with the direct injection of nitrogen (N_2) in TCV. N_2 is injected through a piezo-electric gas valve into the divertor to further cool the exhaust plasma, and we employ the resulting NII (399.5 nm) line emission, cast as an emission front position, to diagnose the plasma detachment progression. Similarly to carbon, nitrogen has a high radiative potential for the temperature range typical of the TCV divertor, where core impurity concentrations may be kept relatively low [10].

We use the transfer function structure derived in [11] for emission front control in TCV, which is based on a 1D diffusion equation. This model is regressed against system identification measurements, as the simple gain and delay model used in [7] was unable to reproduce the measured dynamic response of the CIII emission front to D_2 gas injection [11].

Note that, the nitrogen seeded detachment physics in TCV L-mode plasmas was probed experimentally in [10] and compared with SOLPS-ITER in [12]. In this paper we focus specifically on using the NII emission front position as a control parameter for the divertor plasma, and on designing the required controllers for N_2 and D_2 actuation of this front in a systematic way. Furthermore, we compare the dynamic response of the exhaust plasma to N_2 and D_2 injection to gain further insight for dynamic models for heat exhaust control.

In this paper, we report on three key results: 1) Successful real-time control of the NII emission front position actuated by N_2 gas injection, and actuated by D_2 gas injection including a diagnostic N_2 puff, demonstrating the use of tracer impurity control. A single discharge per actuator was sufficient to identify the transfer function model parameters and design a controller for each of these: N_2 and D_2. This is the first demonstration of real-time control of the plasma exhaust using N_2 in TCV, and the first demonstration of using the transfer function structure of [11] to design a gas injection actuated emission front controller; 2) The controlled NII front position was consistently located $2-3$ cm below the CIII emission front position, hence, the NII emission is indicative of a colder region than the CIII emission. This is qualitatively in line with the SOLPS-ITER analysis of [12], where the CIII and NII impurity emission fronts were found to correspond to a local electron temperature of 11-12 and 6.5 eV respectively, although it should be noted that experimental temperatures (from spectroscopy and Thomson Scattering when available) are generally considerably lower (see e.g. [13] and references therein); 3) The CIII and NII emission front positions respond identically to D_2 or N_2 injection

perturbations in the system identification experiments, indicating they cannot be controlled independently by the used actuators, at least up to the highest excited frequency of 37 Hz. Both fronts do, however, respond differently to actuation using D_2 than to actuation using N_2, with the latter inducing a stronger, but slower response of both fronts.

This paper is organized as follows. In Section 2, the experimental set-up and the control goal, including the used actuators and sensor in the control loop are introduced. In Section 3, the system identification experiments are discussed and their results presented. The system identification results are then used to regress the diffusion-based transfer function structure on which we base the controller design. We show the emission front control results in Section 4, and analyze the impact of NII emission front position on target saturation current density and radiated power fraction. We also compare actuation of the NII emission front using D_2 and N_2 as actuators to track the same desired reference position. The conclusions and a discussion follows in Section 5.

2. Experimental setup

The experiments for this work were performed on the Tokamak à Configuration Variable (TCV) [14]. Results are obtained in a lower single-null 340 kA Ohmically heated diverted L-mode scenario in reversed field (unfavorable to H-mode access), $B_{tor} = 1.4$ T, and a line-averaged electron density of $\hat{n}_e \approx 9 \cdot 10^{19}$ m^{-3} ($f_{GW} = 0.4$). The scenario is similar to the high-density scenario used in [10] to analyze nitrogen seeded divertor detachment in TCV L-mode plasmas and was chosen as it operates close to detachment. Additionally, it was observed in [10] that the higher line-averaged density case resulted in better the core screening to N_2 penetration, increasing the discharge's operational range with respect to the quantity of N_2 injected.

2.1. Control goal

The TCV divertor plasma can be spectroscopically diagnosed from either intrinsic (e.g. carbon, helium, hydrogen) or extrinsic (e.g. nitrogen, argon) line emission [15, 16]. Their emission spectra are strongly temperature-dependent in the divertor plasma temperature range, providing direct information on the divertor plasma state [17].

In this work, we aim to control the NII emission front position, diagnosing the exhaust plasma by using the emission of an injected impurity instead of the intrinsic carbon always present in TCV. We aim to control the NII front with two actuators: 1) Using N_2 gas injection as an actuator, directly changing
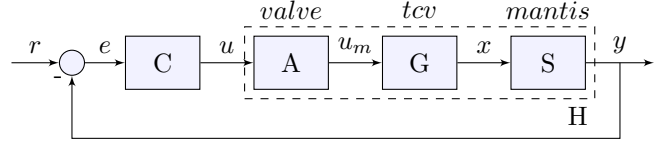

Figure 1: The process control loop. A control reference position r is compared with a measured front position y. The control error e is fed to a controller C, which computes voltage request u, send to the gas valve actuator A. The internal gas valve controller follows this request, resulting in a (measured) injected gas flow u_m. The gas enters the plant G, which is the TCV. The divertor plasma response, in terms of an emission front position, is measured using the sensor S, i.e. MANTIS.

the impurity radiating power intensity whilst having a relatively small effect upon the core plasma density; 2) Using D_2 gas injection as an actuator, increasing the divertor plasma density that also changes the intrinsic carbon source (and subsequent carbon radiation) and the hydrogenic radiated power. Here, we also inject a small amount of N_2, to probe the use of extrinsic impurities as diagnostic tracers.

Unlike CIII emission, whose extinction near the target is often taken as an indication of the onset of divertor detachment in TCV [10, 13, 18, 19] and was used as a control parameter cast as an emission front position in [7], the NII impurity emission front has not yet been used for control purposes. From SOLPS-ITER analysis of [12] and experimental results from [10] the NII emission front position is expected at a lower plasma temperature and therefore positioned between the divertor target and the CIII emission front position. Its extinction near the target is thus an indication of lower divertor temperatures than the extinction of CIII emission.

Figure 1 shows the process control loop. The dynamics of the full system H are defined from requested gas input u to measured NII front position y, that includes the actuator A, the plant G and sensor S. These need to be included to design a feedback controller off-line and predict performance and robustness margins [20]. Next, we elaborate on the used sensor and actuator and their individual dynamics. Identification of the local (linearized) dynamics of the plant G, together with the full system from u to y, is performed through system identification experiments shown in Section 3.

2.2. Sensors

The NII and CIII emission front locations are measured using a real-time detection algorithm [21] applied to spectrally filtered images originating from the multi-spectral imaging diagnostic MANTIS [22]. The

MANTIS cameras run at a frame rate of 800 Hz, where the shutter opening time stamp plus half the exposure time ($\approx$ 0.5 ms) for each image is taken as the representative time for when each image, and thus the front position, is measured. We define the corresponding front position as x_{NII}, which is the total distance from the outer divertor target to the front location, along the outer leg. Conversely, the front position as received by the real-time control system, after the image has traversed the real-time detection and written the result to memory, is defined as y_{NII}. The value for y_{NII} is delayed by 4 ms with respect to x_{NII}. These sensor dynamics S are, thus, well captured by $y(t + 0.004) = x(t)$, which we write in the form of a transfer function as

$$y(s) = \underbrace{e^{-0.004s}}_{S(s)} x(s), \tag{1}$$

with s the Laplace variable. We use the Laplace domain representation, since the total system then becomes a straightforward multiplication of the terms: $G(s) = S(s)H(s)A(s)$, assuming local linearity. This was elaborated in previous work [11] and references therein.

We investigate the effect of the NII emission front position on the divertor plasma from the ion saturation current density at the inner- and outer strike point using wall-embedded Langmuir probes, and from the radiated power measured by gold-foil bolometers [23]. The Langmuir probes provide a measurement of the ion saturation current density from current-voltage curve fits over a 5 ms period average (more details on the analysis are described in [24]). The bolometers estimate the total radiated power fraction $f_{\text{rad}}^{\text{tot}}$ and radiated power fraction in the scrape-off-layer $f_{\text{rad}}^{\text{SOL}}$. Radiated power from the core $P_{\text{rad}}^{\text{core}}$ is estimated from a tomographic reconstruction of the bolometer camera array. We define the total and SOL radiated power fractions as

$$
\begin{aligned}
f_{\text{rad}}^{\text{tot}} &= \frac{P_{\text{rad}}^{\text{tot}}}{P_{\text{ohm}}}, \\
f_{\text{rad}}^{\text{SOL}} &= \frac{P_{\text{rad}}^{\text{tot}} - P_{\text{rad}}^{\text{core}}}{P_{\text{ohm}} - P_{\text{rad}}^{\text{core}}} = \frac{P_{\text{rad}}^{\text{SOL}}}{P_{\text{SOL}}},
\end{aligned} \tag{2}
$$

respectively, where P_{ohm} is the ohmic heating power. Figure 2 shows the positions of the LPs, bolometer lines of sight, and an example of the detected NII emission front position a discharge.

2.3. Actuators

The NII emission front position is controlled by the injection of N_2 or D_2 molecules in the divertor through piezo-electric gas valves [25]. A pressure transducer at the output of the valve is absolutely calibrated to estimate the mass flow entering the vacuum vessel.
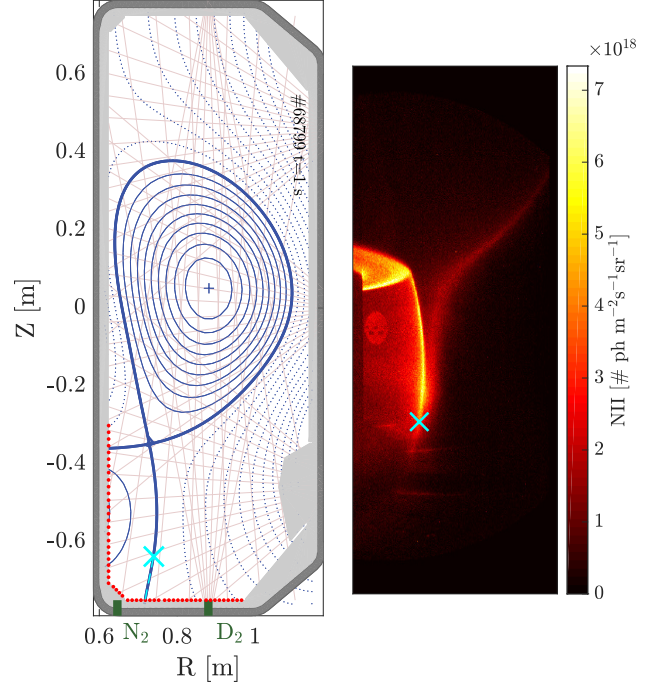

Figure 2: Left: magnetic geometry used for this work is shown in the poloidal plane of TCV in blue. Langmuir probe locations which were used to measure ion saturation current density are shown by red dots. Lines of sight of 64 gold-foil bolometers which were used to estimate radiated power are shown in pink. Gas injection locations of D_2 and N_2 are located at the machine bottom shown in dark green. Right: NII emission image from MANTIS at $t = 1$ s during this discharge, including the detected NII emission front location indicated by the cyan cross. The detected position is mapped to the poloidal plane on the left using the algorithm of [21], resulting in $y_{\text{NII}} = 0.12$ m, which is the total distance from the outer divertor target to the front position along the outer leg.

Both the actuator voltage request u to the valve, and the pressure at the valve output (directly related to gas flow) u_m are measured. The piezo-electric valves have a dynamic response from a requested gas flow to an actual gas flow indicated by the block A in Figure 1. Separate identification of the dynamics of each valve was obtained by step response measurements. Their dynamics were well captured by a first-order plus dead-time (FOPDT) model

$$\dot{u}_m(t)\tau = -u_m(t) + Ku(t - \tau_d), \tag{3}$$

that can be described by the transfer function

$$u_m(s) = \frac{K}{\tau s + 1} e^{s\tau_d} u(s), \tag{4}$$

with model parameters K [-], τ [s] and τ_d [s] that describe the system gain, time constant and delay respectively. The step response of (3) is

$$u_m(t) = \delta K (1 - e^{(t - \tau_d)/\tau}), \tag{5}$$

Table 1: Gas valve model parameters

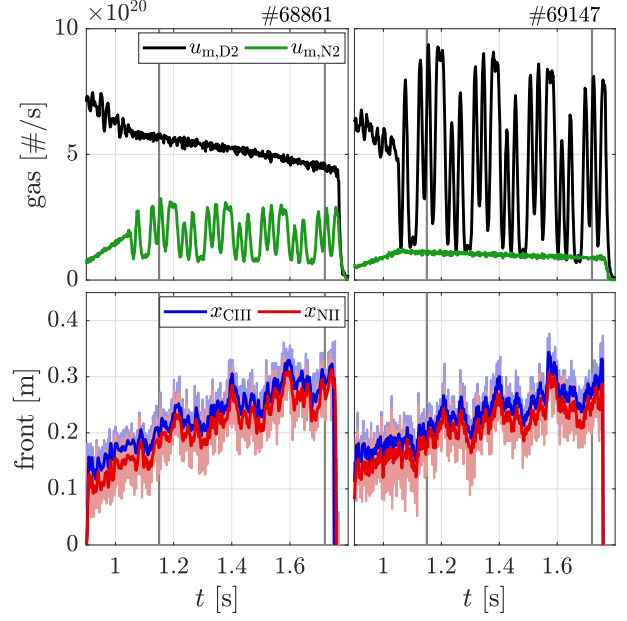| Parameter	N$_2$ valve	D$_2$ valve	unit
K	0.91	0.97	-
τ	2.00	1.12	ms
τ_d	1.90	1.50	ms

Figure 3: Time-traces of the system identification experiments for discharges #68861 (left) and #69147 (right). Top: measured gas injection in molecules per second for both nitrogen ($u_{\mathrm{m,N2}}$) and deuterium ($u_{\mathrm{m,D2}}$). Bottom: measured impurity front position of CIII and NII compensated for the 4 ms time-delay of the sensor dynamics. A filtered measurement, using a IIR low pass filter with 40 Hz passband edge frequency, is shown on top of the raw measurement for clarity of the response in the time-domain.

where δ is the applied step input on u. The model parameters K, τ and τ_d are determined by regressing the FOPDT model on 15 step response measurements in the time-domain, using a root-mean-squared (RMS) error minimization of the modeled step-response with respect to the measured response.

Table 1 shows the average of the obtained model parameters for each valve over the 15 measurements. We shall refer to the corresponding models as $A_{D2}(s)$ and $A_{N2}(s)$ for the deuterium valve and the nitrogen valve, respectively. Figure 2 shows the gas injection locations of both these valves in TCV.

3. System identification experiments

Efficient and systematic controller design requires a dynamic model of the to-be-controlled system [6], herein the total dynamics from input u to output y as shown in Figure 1. In reality, most systems have nonlinear input/output characteristics, however, a local linear description is often sufficient to describe the dynamics within a useful operating range [26], where the feedback controller will deal with residual nonlinearities. These local system dynamics are identified experimentally using dedicated system identification experiments, similar to [7, 27]. By exciting the system with carefully designed perturbations to the input u while measuring the output y, assuming small perturbations, a local linear approximation of the system is identified. This local description is only valid for an operating range around the perturbed equilibrium, whose size depends on the strength of present non-linearities. In [7] no clear non-linear contributions were identified from dedicated system identification experiments using D$_2$ gas perturbations to perturb the CIII emission front position, providing confidence that a local linear description is adequate for emission front controller design.

As described in Section 2, we can measure the mass flow of gas entering the vessel, and also the shutter aperture time of MANTIS and corresponding front position measurement x. We can therefore identify the local dynamics of the plant, $\hat{G}(s)$, individually as well as the local dynamics of the total system $\hat{H}(s) = A(s)\hat{G}(s)S(s)$. We will use this to compare the local response of the divertor plasma to D$_2$ and N$_2$ gas injection without including any spurious effects from the actuator or sensor dynamics,

i.e. comparing the plant physics only. With the actuator and sensor dynamics $A(s)$ and $S(s)$ taken as global descriptions to be valid for the full operational space. For the gas valves known to be untrue when operating near its closure, as its response becomes nonlinear, but we shall assume this contribution to be negligible.

In the following section, the perturbation design for the system identification experiments is briefly discussed, and the experimental results are presented.

3.1. Perturbation design

We identify $\hat{H}(s)$ and $\hat{G}(s)$ in the form of frequency response function (FRF) data, obtained using sinusoidal perturbations superimposed on a pre-programmed feedforward trace. An FRF datapoint is obtained for each frequency ω [rad/s] excited in the perturbation waveform, consisting of the relative amplitude and relative phase of the measured output response to the input perturbation. The FRF datapoints are the evaluation of the system its transfer function in the Fourier domain using $s = j\omega$, which may be interpreted as its response to constant amplitude oscillations. The perturbation we apply to the gas input

is a multisine waveform, consisting of a sum of sinusoids, each with a distinct frequency, phase and amplitude. More information on the specific design of this approach with multisine perturbations in TCV experiments is described in [7], with more information on the general theory available in [27, 28].

The discharge scenario allows for a perturbation time τ_{exp} of approximately $0.8\,$s, placing a lower bound on the identifiable frequency range, or fundamental frequency f_0, at $3.75\,$Hz as a minimum of three periods is required to obtain a meaningful variance computation [28]. We choose to perturb the system using a multisine with $f_0 = 1/0.19\,$Hz and harmonics on lines $1, 3, 5, 7$ ($5.26, 15.79, 26.32, 36.84\,$Hz), applied to the N_2 valve and D_2 valve in discharges #68861 and #69147, respectively. A slightly higher frequency than $3.75\,$Hz is chosen such that earlier than expected plasma discharge termination would include at least three periods of perturbation, ensuring more discharges were effective.

3.2. Experimental results

Figure 3 shows the time traces of the two system identification discharges. The perturbations are superimposed on a designed feedforward trace that provides approximately constant line-averaged density. We observe a clear response of both the NII and CIII emission front to perturbations applied to the N_2 and D_2 valves, including a slow drift of the front position upward along the divertor leg towards the x-point. This drift is a transient response, likely caused by nitrogen impurity accumulation in the plasma and/or changing wall sources and sinks, for which we compensate in the frequency domain analysis using the local polynomial method [27]. We find the CIII emission front position is consistently located $2-3\,$cm above the NII emission front position throughout the discharge, demonstrating the NII front is indicative of a colder region than for CIII assuming a negative temperature gradient from upstream to target.

We analyze the frequency response measurements by plotting the FRF datapoints in a Bode plot, that shows the relative amplitude and phase between input perturbation and output response. Figure 4 shows the measured frequency response function (FRF) data points from both actuators (actual N_2 and D_2 gas flow) to the CIII and NII emission front positions compensated for the $4\,$ms measurement delay, i.e. these results are corrected for actuator and sensor dynamics (cf. $G(s)$ only in Figure 1).

The FRF data shows that both the CIII and NII emission fronts respond equally to the perturbations on a single actuator, i.e. they move together when a single gas species is perturbed. Until the highest probed excitation frequency of $36.84\,$Hz, no clear separation
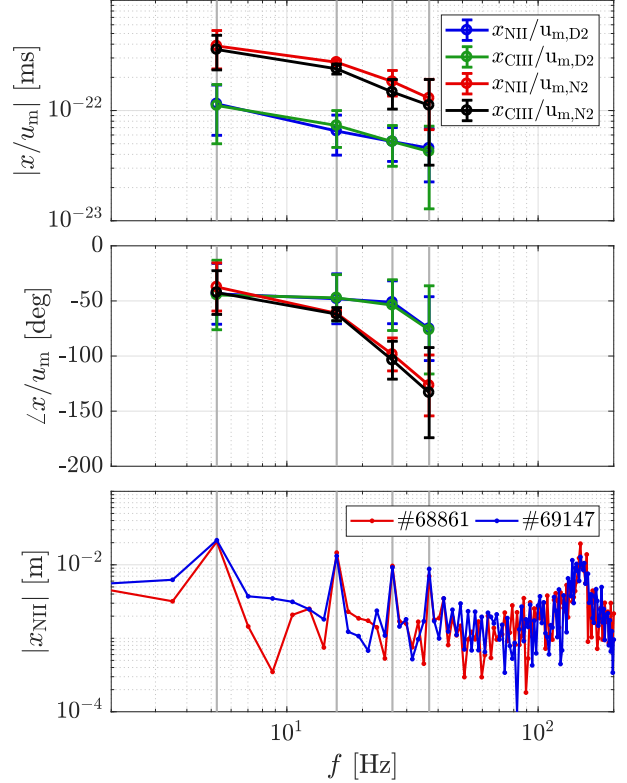

Figure 4: Results of the system identification experiments in the frequency domain. Top and middle: FRF measurement results of the CIII and NII emission front responses to nitrogen ($u_{\mathrm{m,N2}}$) and deuterium ($u_{\mathrm{m,D2}}$) shown in a Bode plot. Results are compensated for non-periodic behavior like transients using the local polynomial method as described in [27]. The 2σ errorbars are computed using the propagation of uncertainty for magnitude and phase as in [29], assuming a noiseless input case. Bottom: discrete Fourier transform (DFT) of the NII emission front response to both gas species, the signal has been compensated for the slow drift (using linear detrending) for clarity. The grey vertical lines indicate the excited frequencies in the perturbation.

of these fronts is seen, implying emission equilibration time-scales in the scrape-off layer are significantly faster.

With N_2 perturbations, we observe a stronger phase drop and an amplitude response of almost a factor four higher, per molecule, than with D_2. Thus, N_2 injection results in a stronger, although for higher ($> 10\,$Hz) frequencies slower, response of the NII and CIII emission front positions than D_2.

Figure 4 also shows the discrete Fourier transform (DFT) of the NII emission front response amplitude over frequency. The perturbed frequency amplitudes are clearly well above the noise level, with a strong peak observed around $\sim 150\,$Hz. This periodic external disturbance (not resulting from the applied

perturbations) is concentrated around the sawteeth crash frequency for this scenario, determined from soft X-ray emission measurements. Sawteeth perturb the core plasma, and are some time later observed in the divertor plasma. They do not effect the system identification results, as it is significantly removed from the probed excitation frequencies. However, this observation will be retained in controller design, to ensure it does not act on these high frequency disturbances.

In the next section we obtain a model of the full system H, by coupling the estimated actuator and sensor dynamics $A(s)$ and $S(s)$ to our local plant dynamics $\hat{G}(s)$. The resulting model $\hat{H}(s) = S(s)\hat{G}(s)A(s)$ is then verified experimentally using FRF measurements.

3.3. Transfer function model

In section 2, the sensor and actuator dynamics of our control loop were introduced as the transfer functions $S(s)$ for the MANTIS real-time front detection and A_{D2}, A_{N2} for the deuterium and nitrogen gas valve dynamics respectively. The NII emission front response is found to be different for each actuator, so a separate transfer function models of the local plant approximation $\hat{G}_{D2}(s)$ and $\hat{G}_{N2}(s)$ is taken to describe the response to deuterium and nitrogen. A control-oriented transfer function model structure for emission front control in TCV was presented in [11]. This model is based on the observation of typical Warburg-domain phase and magnitude behavior of FRF measurements from D_2 gas injection to CIII front position response, indicating a (quasi) diffusive process can describe the plant dynamics.

We reuse this model here, assuming a (quasi) diffusive process is appropriate to describe the dynamic response to N_2 gas injection. As in [11] we take a direct relation between the change in local neutral density and front position, but allow the evaluation location of this neutral density to vary. The transfer function structure for $\hat{G}(s)$ then becomes

$$\delta y = \frac{\cosh(\hat{x}\lambda)\tanh(L\lambda) - \sinh(\hat{x}\lambda)}{D\lambda}\delta u \qquad (6)$$

where $\hat{x}$, L and D represent the evaluation location, domain size and diffusion coefficient respectively, and $\lambda = \sqrt{s/D}$ with s the Laplace variable. Note that, we use here δu and δy as the model is a local (linearised) approximation of the dynamics. As the valve reference u is in units of volts, the other parameter magnitudes are no longer physical parameters, but merely the structure of the function is used. One of the problems addressed in [11] with identifying such parameters with system identification data is the limited range of frequencies that can be identified. Specifically, a lower

Table 2: Plant model parameters

Parameter	G_{N2}	G_{D2}	unit
D	4.424	17.136	m^2s^{-1}
$\hat{x}$	0.249	0.054	m
L	0.427	2.625	m

limit is induced by the experimental time duration as discussed at the start of this section. Additional data is required to obtain a unique parameter fit, which was obtained in [11] using SOLPS-ITER simulations to obtain an additional FRF data point at the zero-frequency that represents the DC-gain. We re-use this data point, together with the conversion factor for molecules per second to volts which is different for each gas valve. The DC-gain for $\hat{G}_{D2}(s)$ then becomes $0.15\,\text{mV}^{-1}$ corresponding to $4.22 \times 10^{-22}\text{m/D}_2\text{s}^{-1}]$ in our operating space. For $\hat{G}_{N2}(s)$, such analysis with SOLPS-ITER has yet to be performed. We, therefore, analyze the change in NII emission front position to step-wise increases from N_2 injection in a preceeding discharge. The change in NII emission front position was $0.042\,\text{mV}^{-1}$ for N_2 injection, which we use as the DC-gain for $G_{N2}(s)$. The resulting model parameters, after regression to the measurements, are shown in Table 2. Figure 4 shows the used DC-gains by dashed lines.

Now that the individual models of the process loop in Figure 1 are known, we can take their product (assuming local linearity) to obtain models for the full system as

$$\delta y_{NII} = \underbrace{A_{N2}(s)G_{N2}(s)S(s)}_{H_{N2NII}}\delta u_{N2}(s),$$
$$\delta y_{NII} = \underbrace{A_{D2}(s)G_{D2}(s)S(s)}_{H_{D2NII}}\delta u_{D2}(s). \qquad (7)$$

These should coincide with our FRF measurement of the full system $\hat{H}(s)$ for both cases. Figure 5 shows that this is indeed the case, as our derived transfer function models of the full system reproduces the FRF measurements, confirming that the transfer function models of (7) adequately capture the system dynamics. The transfer functions $\hat{H}_{N2NII}(s)$ and $\hat{H}_{D2NII}(s)$ may thus be used to design a controller for both actuators to control the NII emission front position in real-time. Evidently, we could have fitted a model directly from the FRF measurements of $\hat{H}(s)$, equally useful for controller design. However, separating the control loop into several sub-models provides more insight into the performance of each system component. This allows, for example, to replacement of the gas valve actuator to directly observe the resulting effect on performance with an equivalent controller, or use it to design a new controller. Furthermore, it allows the
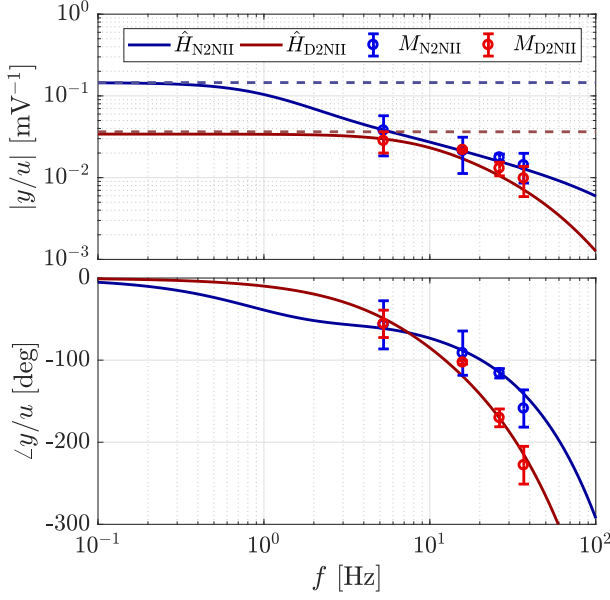
Figure 5: Bode plot of the transfer function models $\hat{H}_{\mathrm{N2NII}}(s)$ and $\hat{H}_{\mathrm{D2NII}}(s)$ and the FRF measurements of the full system from u (gas valve reference) to y (NII front position) in the case of D_2 and N_2 gas perturbation, indicated by $M_{\mathrm{D2NII}}(s)$ and $M_{\mathrm{N2NII}}(s)$ respectively. The dashed lines indicate the DC-gain used to regress the $G(s)$ models multiplied by the DC-gain of the valve and sensor, i.e. $\hat{H}_{\mathrm{N2NII}}(0)$ and $\hat{H}_{\mathrm{D2NII}}(0)$.

direct comparison of the measured plasma response to machines and experiments where different actuators or sensors are used.

4. Control experiments

In this section, we present the NII emission front control results. We start with details on the controller design, present the experimental result for two discharges, and finally compare D_2 and N_2 actuation from two discharges with identical NII emission front position control references.

4.1. Controller design

The controllers are designed using the Loop Shaping method [20]. As the system is gas transport driven, we do not expect any resonances and should obtain adequate performance from a PI controller. A PI controller of the form

$$C(s) = K_{\mathrm{p}} \frac{s + K_{\mathrm{i}}}{s} \tag{8}$$

is chosen for both actuators, where the controller gain K_p and integrator cut-off frequency K_i are chosen such that a bandwidth of $7\,\mathrm{Hz}$ is obtained with a phase margin of 50 degrees or higher to maintain sufficient robustness margin for modeling errors whilst limiting

Table 3: *Controller design parameters*

Parameter	$C_{\mathrm{D2}}(s)$	$C_{\mathrm{N2}}(s)$	unit
K_{p}	12	15	-
K_{i}	24π	24π	rad/s
bandwidth	7	7	Hz
phase margin	53	62	deg.

overshoot. A bandwidth of $7\,\mathrm{Hz}$ has proven sufficient to provide reasonable performance for emission front control as shown in [7]. The controller is extended using an Infinite Impulse Response (IIR) low pass filter with a passband edge frequency at $40\,\mathrm{Hz}$, to reduce the influence of high-frequency measurement noise like the measured $\sim 150\,\mathrm{Hz}$ peak originating from sawtooth crashes (see Figure 4) on the tracking error. We choose an IIR low-pass filter as this meets the filter specifications with a lower filter order than Finite Impulse Response filters, leading to lower computation and storage costs in the control system [30]. The filter must be accounted for during loop shaping, by taking the product of the transfer function of the low-pass filter and the PI controller. Table 3 shows the resulting controller gains, bandwidth and phase margin. The controllers are implemented with the clamping anti-windup method to prevent integral windup.

4.2. Experimental results

Figure 6 shows two discharges where the NII emission front position was controlled using N_2 seeding. In discharge #69144 a step-wise increase in the control reference was applied, we find the controller is able to track the desired reference well with little overshoot after the step transitions. The resulting peak target current density J_{sat}^{peak} follows an inverse response, showing a clear reduction when the NII front is at a higher position in the divertor leg. Additionally, both the total radiated power fraction $P_{\mathrm{total}}^{\mathrm{rad}}/P_{\mathrm{ohm}}$ and the radiated power fraction in the SOL $P_{\mathrm{SOL}}^{\mathrm{rad}}/P_{\mathrm{SOL}}$ show a correlated increase with NII front position height.

In discharge #69185 a step-wise increase in NII front reference position is requested first, followed by a step decrease. The controller is again well able to track the desired reference for the step increase, but the front remains too high after the step decrease, even though the controller ceases N_2 injection completely. Like the NII front position, the radiated power fractions does not decay further after $1.4\,\mathrm{s}$, although, again, N_2 seeding has ceased completely. Interestingly, the peak target current density continuous to increase after this time, possibly caused by the observed increase in line-averaged density after seeding has ceased. In attached conditions of TCV L-mode plasmas, the target ion flux scales linearly with line-averaged density [13, 15]. To
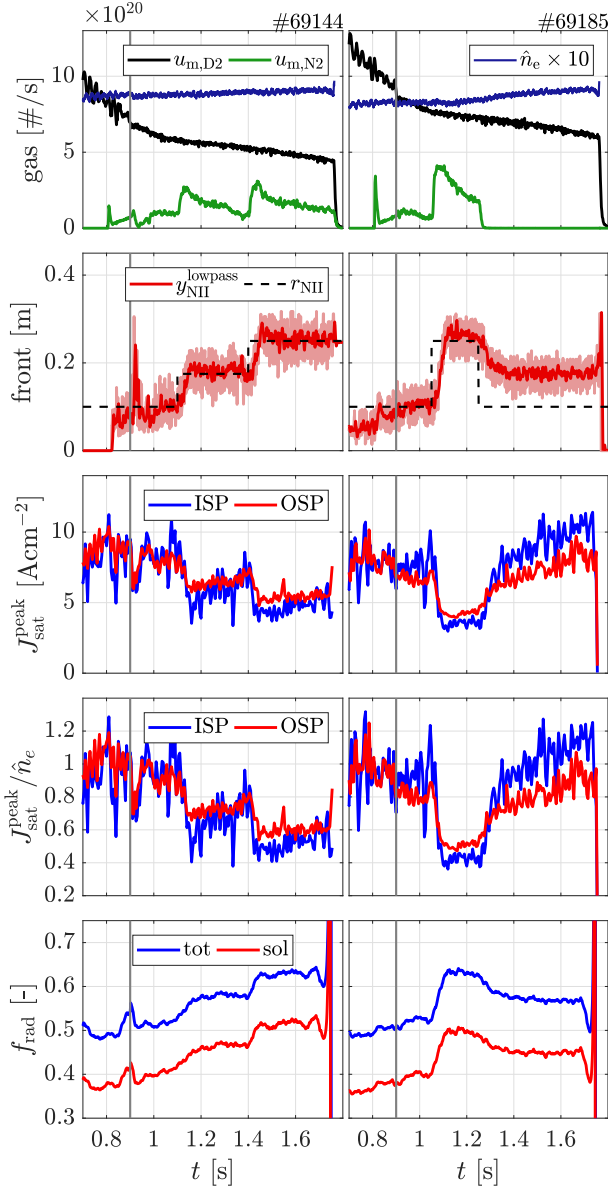
Figure 6: Experimental results for two reference tracking experiments of the NII emission front using first N_2 seeding. Row 1: injected N_2 and D_2 gas and line-averaged electron density $\hat{n}_e$. Row 2: requested front position reference r_{NII} and both raw and low-pass filtered measured front position y_{NII}. Row 3: peak target current density J_{sat}^{peak} on the inner strike point (ISP) and outer strike point (OSP). Row 4: Ratio of J_{sat}^{peak} to $\hat{n}_e \cdot 10^{19}$. Row 5: total radiated power fraction P_{total}^{rad}/P_{ohm} and SOL radiated power fraction P_{SOL}^{rad}/P_{SOL}.

disentangle the effect of density changes to J_{sat}^{peak}, we analyze traces of $J_{sat}^{peak}/\hat{n}_e \cdot 10^{19}$, that show a smaller, but still clear, increase after N_2 seeding ceases.
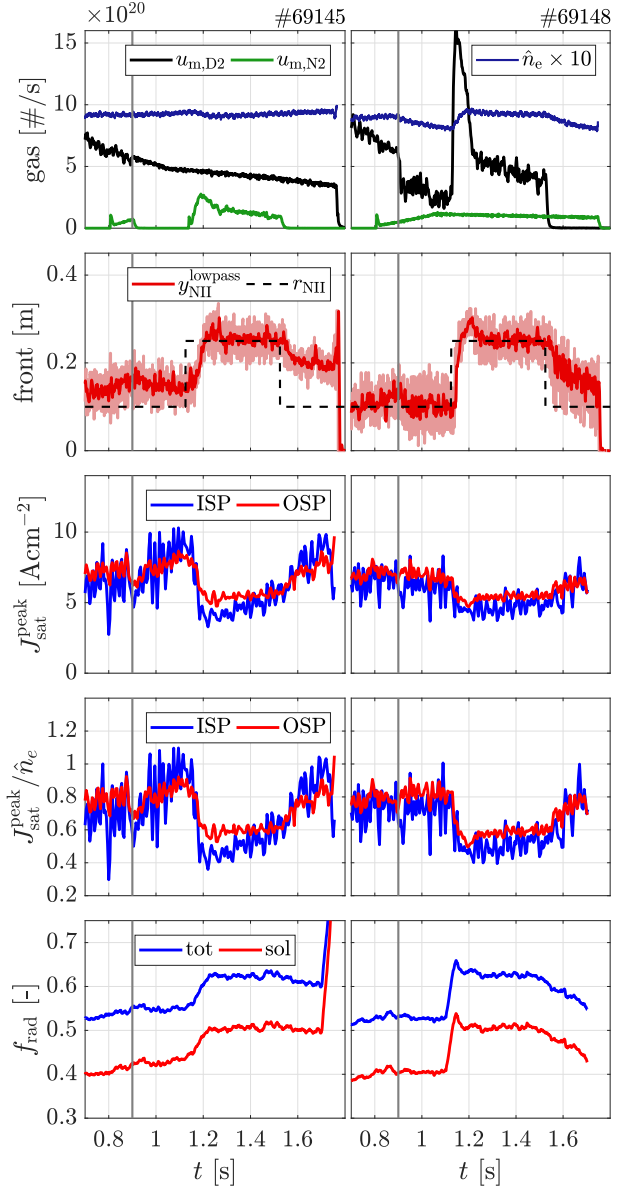
Figure 7: Experimental results for equal reference tracking of the NII emission front using N_2 (#69145) and D_2 (#69148) as an actuator. Traces as in Figure 6.

4.3. Comparison of deuterium and nitrogen actuation

Figure 7 compares two discharges where the NII emission front position was controlled towards an identical reference trajectory, using N_2 seeding (#69145) or using D_2 fueling (#69185) as an actuator. With D_2 fueling a small constant influx of N_2 is maintained as a trace impurity, to ensure the NII impurity emission front can remain detectable.

The controller tracks the step-wise increase of the desired front position well for both cases. However, here again the step decrease has difficulties. For N_2 actuation the NII front position remains higher than

desired, even though the N_2 valve is closed and the line-averaged electron density is no longer increasing. For D_2 actuation the NII front position again remains higher than desired, with the D_2 valve closed. Here, however, this is accompanied by a clear decrease in emission front position, in line with the decay in line-averaged density and radiated power fractions that accompany the reduced gas injection. The peak target current density J_{sat}^{peak} shows a considerably different behavior. A clear reduction is obtained with a higher NII front position for N_2 actuation alone, which is attributed to a reduction in ionization efficiency from the SOLPS-ITER analysis in [12]. In contrast, D_2 actuation does not show this reduction. We note that moving the NII front position with D_2 actuation is coherent with the change in line-averaged density, leading to relative constant J_{sat}^{peak}, likely resulting from operating around a line-averaged density close to pre-detachment roll-over for this scenario [10]. This is confirmed by accounting for changes in line-averaged density by comparing the traces of $J_{\text{sat}}^{peak}/\hat{n}_e$, showing fairly equal changes for both D_2 and N_2 actuation.

5. Conclusion and discussion

In this work, we have shown the first results of real-time control of the NII (399.5 nm) emission front position using N_2 seeding in TCV, diagnosing the exhaust plasma by using light emission of an injected impurity gas. We used a novel control-oriented transfer function structure for emission front control in TCV [11], regressed onto system identification measurements to obtain a (locally valid) dynamic model of the NII front response to both D_2 and N_2 gas injection. This model was combined with an identified model for the gas valve actuators, and for the MANTIS sensor, to construct a model description of the complete system dynamics, subsequently used to design controllers off-line, providing successful control of the following discharge.

We have demonstrated real-time control of the NII emission front position actuated by N_2 gas injection, or actuated by D_2 gas injection while injecting a small amount of N_2 as a trace impurity. For both cases, the NII emission front was controlled towards higher positions, but moving the front position back towards the target proved difficult, likely affected by nitrogen retention in the machine. This retention was observed to affect subsequent discharges, showing the importance of tracking impurity concentrations and efficient impurity removal. If impurity injection is used to mitigate radiative fluctuations in the plasma exhaust this accumulation would become a limiting factor in control performance, strategies where impurity injection is kept to a minimum would be required. This

is inline with the strategic operation of exhaust control, that must simultaneously encompass a soft limit of re-attachment (which can still be temporarily endured by using, for example, strike-point sweeping [31, 32]), and a hard limit resulting from radiative instability induced disruptions.

We found the NII front position is consistently located between the CIII emission front and the divertor target, showing the NII front position is indicative of a colder plasma region than its CIII counterpart. This is qualitatively in line with the SOLPS-ITER analysis of [12], where the CIII and NII impurity emission front was found to correspond to a local electron temperature of 11-12 and 6.5 eV respectively, where it should be recalled that experimental measurements of the CIII emission front temperature are considerably lower (see e.g. [13]). We have shown the CIII and NII emission front positions respond simultaneously to the injection of D_2 or N_2 perturbations in the described system identification experiments, indicating these front positions cannot be controlled independently by the used actuators, at least up to the highest probed excited frequency of 37 Hz.

However, both emission fronts do respond differently to D_2 actuation than to N_2 actuation, where the latter induces a stronger, but slower response of both front positions. We note that N_2 is injected in the private flux region, while D_2 is injected in the open flux region, possibly partly explaining the difference in response. However, the frequency response measurements in [7] using D_2 injection in the private flux region show similar results as the results of D_2 injection presented here. This leads us to conjecture that differences in transport and thermal velocity due to mass difference may be a more reasonable candidate to explain this difference in response, but further investigation is necessary.

We note that, even after completely ceasing N_2 or D_2 injection, pre-seeding/fueling conditions were not obtained before the end of the discharge, likely caused by insufficient N_2 impurity removal and/or decay-time of divertor plasma density respectively. However, [7] demonstrated the displacement of the CIII emission front from the target and back twice using D_2 in an unseeded TCV discharge with a similar controller, showing faster movement of an impurity emission front back to the target than observed in this work. Leaving one of the actuators (N_2 or D_2) uncontrolled may be the cause of this discrepancy, unintentionally increasing impurity enrichment in the case of D_2 actuation instead of merely having a trace impurity. A combination of real-time D_2 and N_2 actuation to control the divertor state more appropriately may be required, complemented by an additional measurement next to an impurity emission front position, for

example tracking impurity retention. As both D_2 injection and N_2 injection affect the impurity emission front position in separate ways, this will require a controller that specifically handles this interaction. Such a multi-input multi-output (MIMO) controller is presently under development at TCV.

Acknowledgments

References

[1] H. Zohm et al. On the physics guidelines for a tokamak DEMO. *Nucl. Fusion*, 53(7):073019, jul 2013.

[2] A. Loarte et al. Progress in the ITER Physics Basis Chapter 4: Power and particle control. *Nucl. Fusion*, 47(6):203, 2007.

[3] R. A. Pitts et al. Physics basis for the first ITER tungsten divertor. *Nucl. Mater. Energy*, 20(August):100696, 2019.

[4] B. Lipschultz et al. Sensitivity of detachment extent to magnetic configuration and external parameters. *Nucl. Fusion*, 56(5):56007, 2016.

[5] T. Donné. European Research Roadmap to the Realisation of Fusion Energy. *EUROfusion*, 2018.

[6] G. F. Franklin et al. *Feedback Control of Dynamical Systems*. Pearson, New York, 8th edition, 2019.

[7] T. Ravensbergen et al. Real-time feedback control of the impurity emission front in tokamak divertor plasmas. *Nat. Commun.*, 12(1):1–9, 2021.

[8] A. Kallenbach et al. Impurity seeding for tokamak power exhaust: from present devices via ITER to DEMO. *Plasma Phys. Control. Fusion*, 55(12):124041, dec 2013.

[9] C. Guillemaut et al. Real-time control of divertor detachment in H-mode with impurity seeding using Langmuir probe feedback in JET-ITER-like wall. *Plasma Phys. Control. Fusion*, 59(4):1–7, 2017.

[10] O. Février et al. Nitrogen-seeded divertor detachment in TCV L-mode plasmas. *Plasma Phys. Control. Fusion*, 62(3):035017, 2020.

[11] J. Koenders et al. Systematic extraction of a control-oriented model from perturbative experiments and SOLPS-ITER for emission front control in TCV. *Nucl. Fusion*, 62(6):066025, jun 2022.

[12] A. Smolders et al. Comparison of high density and nitrogen seeded detachment using SOLPS-ITER simulations of the tokamak á configuration variable. *Plasma Phys. Control. Fusion*, 62(12):125006, dec 2020.

[13] C. Theiler et al. Results from recent detachment experiments in alternative divertor configurations on TCV. *Nucl. Fusion*, 57(7):072008, 2017.

[14] H. Reimerdes et al. Overview of the TCV tokamak experimental programme. *Nucl. Fusion*, 62(4):042018, apr 2022.

[15] K. Verhaegh et al. An improved understanding of the roles of atomic processes and power balance in divertor target ion current loss during detachment. *Nucl. Fusion*, 59(12):126038, 2019.

[16] A. Perek et al. Measurement of the 2D emission profiles of hydrogen and impurity ions in the TCV divertor. *Nucl. Mater. Energy*, 26(November 2020):100858, mar 2021.

[17] A. Perek et al. A spectroscopic inference and SOLPS-ITER comparison of flux-resolved edge plasma parameters in detachment experiments on TCV. *Nucl. Fusion*, 62(9):096012, sep 2022.

[18] J. R. Harrison et al. Detachment evolution on the TCV tokamak. *Nucl. Mater. Energy*, 12:1071–1076, 2017.

[19] J. R. Harrison et al. Progress toward divertor detachment on TCV within H-mode operating parameters. *Plasma Phys. Control. Fusion*, 61(6):065024, 2019.

[20] S. Skogestad and I. Postlethwaite. *Multivariable Feedback Control—Analysis and Design*. John Wiley & sons, New York, second edition, 2007.

[21] T. Ravensbergen et al. Development of a real-time algorithm for detection of the divertor detachment radiation front using multi-spectral imaging. *Nucl. Fusion*, 60(6):066017, 2020.

[22] A. Perek et al. MANTIS: A real-time quantitative multispectral imaging system for fusion plasmas. *Rev. Sci. Instrum.*, 90(12):123514, 2019.

[23] I. Furno et al. Fast bolometric measurements on the TCV tokamak. *Rev. Sci. Instrum.*, 70(12):4552–4556, dec 1999.

[24] O. Février et al. Analysis of wall-embedded Langmuir probe signals in different conditions on the Tokamak à Configuration Variable. *Rev. Sci. Instrum.*, 89(5), 2018.

[25] S. C. Bates and K. H. Burrell. Fast gas injection system for plasma physics experiments. *Rev. Sci. Instrum.*, 55(6):934–939, 1984.

[26] J. Hespanha. *Linear Systems Theory*. Princeton University Press, New Jersey, 2009.

[27] M. van Berkel et al. Correcting for non-periodic behaviour in perturbative experiments: Application to heat pulse propagation and modulated gas-puff experiments. *Plasma Phys. Control. Fusion*, 62(9):094001, 2020.

[28] R. Pintelon and J. Schoukens. *System Identification - A Frequency Domain Approach*. John Wiley and Sons, Hoboken (NJ), 2nd edition, 2012.

[29] M. van Berkel. *Estimation of heat transport coefficients in fusion plasmas*. PhD thesis, 2015.

[30] S. R. Sutradhar et al. IIR based digital filter design and performance analysis. In *2017 2nd Int. Conf. Telecommun. Networks*, volume 2018-Janua, pp. 1–6. IEEE, aug 2017.

[31] G. Maddison et al. Demonstration of real-time control of impurity seeding plus outboard strike-point sweeping in JET ELMy H-mode plasmas. *Nucl. Fusion*, 51(8):082001, aug 2011.

[32] J. Horacek et al. Feasibility study of fast swept divertor strike point suppressing transient heat fluxes in big tokamaks. *Fusion Eng. Des.*, 123:646–649, nov 2017.